Microscopic measurement of the linear compressibilities of two-dimensional fatty acid mesophases.

Cécile Fradin[1], Jean Daillant[1], Alan Braslau[1], Daniel Luzet[1], Michel Alba,[1]

Michel Goldmann[2,3]

[1] Service de Physique de l'Etat Condensé, CEA Saclay,

F-91191 Gif-sur-Yvette Cedex, France.

[2] LURE, F-91405 Orsay Cedex, France.

[3] Laboratoire Physico-Chimie Curie, Institut Curie,

11 rue Pierre et Marie Curie, 75231 Paris Cedex 05.

February 1, 2008

Abstract

The linear compressibility of two-dimensonial fatty acid mesophases has been determined by grazing incidence x-ray diffraction. The unit cell parameters of the L_2, L_2', L_2'', S and CS phases of behenic acid $CH_3 - (CH_2)_{20} - COOH$ and of the L_2 phase of myristic acid $CH_3 - (CH_2)_{12} - COOH$ were determined as a function of surface pressure and temperature. Surface pressure vs molecular area isotherms were reconstructed from these measurements, and the linear compressibility (relative distortion along a given direction for isotropic applied stress) was determined both in the sample plane and in a plane normal to the aliphatic chain director (transverse plane). The linear compressibilities range over two orders of magnitude from 0.1 to 10 m/N and are distributed depending on their magnitude in 4 different sets which we are able to associate with different molecular mechanisms. The largest compressibilities (10 m/N) are observed in the tilted phases. They are apparently independent on the chain length and could

be related to the reorganization of the headgroup hydrogen-bounded network, whose role should be revalued. Intermediate compressibilities are observed in phases with quasi long-range order (directions normal to the molecular tilt in the L_2 or L_2' phases, S phase, and could be related to the ordering of these phases. The lowest compressibilities are observed in the solid untilted CS phase and for one direction of the S and L_2'' phases. They are similar to the compressibility of crystalline polymers and correspond to the interactions between methyl groups in the crystal. Finally, negative compressibilities are observed in the transverse plane for the L_2' and L_2'' phases and can be traced to subtle reorganizations upon untilting.

PACS:

61.10-i   X-ray diffraction and scattering.

68.10.Et Fluid surfaces and fluid-fluid interfaces; interface elasticity, viscosity and viscoelasticity.

68.60.Bs Physical properties of thin films, nonelectronic, mechanical and acoustical properties.

Short title: *Linear compressibilities of two-dimensional mesophases.*

E-mail: *daillant@spec.saclay.cea.fr*

1 Introduction

The organization and phase transitions of Langmuir films, i.e. insoluble amphiphilic monolayers at the air/water interface are strongly affected by the dimension 2 [1, 2]. Considerable effort has been directed during the last few years towards the determination of the structure of the different phases of those systems by grazing incidence x-ray diffraction (GID)[3, 4, 5, 6]. On the theoretical side, many aspects of the phase transitions can be understood using a recently developed Landau theory [7, 8], and realistic simulations are now available [9, 10].

Beyond the great achievement that was the determination of the two-dimensional structure of Langmuir films, a next step, to which simulations contribute, is the understanding of the role of intermolecular forces and conformational defects. Obviously, the elastic properties of monolayers crucially depend on both potentials and defects and their understanding in terms of basic interactions and chain conformations is a challenging goal. Up to now, only the two-dimensional compression and shear elastic moduli have been the subject of detailed studies. For example, the shear modulus has been determined by directly applying the shear to a large polycrystalline sample [11], bending a monocrystal [12], or analysing the shape of Bragg singularities [1, 2]. Because of their inhomogeneity, the elastic moduli obtained with large polycrystalline samples are much smaller than those obtained with monocrystals. This is also true for the compression modulus. This was recognized by Bommarito et al. [6] who determined the compression modulus in different phases of behenic acid by measuring the surface pressure using a Wilhelmy balance and the molecular area from GID data. Another problem shared by all these studies (with a notable exception [13]) is that the anisotropy of the monolayer is not considered, preventing a precise understanding in terms of microscopic structure. In this study, we extend the method of Ref.[6] to determine the linear compressibilities of two different fatty acids, while addressing the anisotropy of the monolayer. This is possible because the GID measurements allow the determination of the two-dimensional lattice parameters, the monolayer thickness and the molecular tilt.

2   Linear Compressibility of a 2D crystal

The surface (volume) compressibility χ of a 2D (3D) crystal is defined as the relative diminution of its area (volume) A when submitted to a pressure Π: $\chi = -1/A(\partial A/\partial \Pi)$. A linear compressibility can also be defined along each direction i as: $\chi_i = -1/u_i(\partial u_i/\partial \Pi)$, where u_i is a length along the direction i. In a non-isotropic medium, the linear compressibility depends on the direction, and can give hints about microscopic phenomena. This has been successfully applied to polymer crystals [14], where information about molecular interactions was obtained by comparing measurements and calculations of the Young modulus and of the linear compressibility along the different crystal axes.

The compressibility can be expressed as a function of the coefficients of the rank 4 elastic tensor s_{ijkl} relating the strain tensor $u_{ij} = 1/2\,(\partial u_i/\partial x_j + \partial u_j/\partial x_i)$, describing the relative distortion of the crystal, and the stress tensor σ_{ij} [15] :

$$u_{ij} = s_{ijkl}\sigma_{kl} \tag{1}$$

(summation over repeated indices is assumed).

The volume compressibility is $\chi = u_{ii}/\Pi$ if Π is the applied isotropic pressure. The linear compressibility in the direction of the unit vector $\boldsymbol{\epsilon}$ is: $\chi_{\boldsymbol{\epsilon}} = u_{ij}\epsilon_i\epsilon_j/\Pi$. The pressure Π applied to our systems is on average[16] a 2D lateral isotropic pressure, so that, if we take $\mathbf{x_1}$ and $\mathbf{x_2}$ in the plane of the sample, the stress tensor becomes :

$$\sigma_{ij} = -\Pi\delta_{ij}. \tag{2}$$

(δ is Kronecker's symbol). Hence $u_{ij} = -\Pi(s_{ij11} + s_{ij22})$, and

$$\chi_{\boldsymbol{\epsilon}} = (s_{ij11} + s_{ij22})\epsilon_i\epsilon_j. \tag{3}$$

Owing to its symmetry properties, the rank 4 elastic tensor s_{ijkl} can be represented by a 6×6 symmetrical matrix s_{ij} with the following correspondance rules: $11 \rightarrow 1$, $22 \rightarrow 2$, $33 \rightarrow 3$, 23 and $32 \rightarrow 4$, 13 and $31 \rightarrow 5$, 12 and $21 \rightarrow 6$ [15].

The crystals under consideration here can alternately be viewed as very thin three-dimensional crystals if their properties along the vertical direction are considered or as two-dimensional crystals if we are only interested in their in-plane properties. Of course, the 3D description is more complete and rich.

All the studied mesophases are either monoclinic (L_2, L_2', L_2'') or orthorombic (S and CS) (cf Fig.1). Whereas the monoclinic elastic matrix has 13 independent coefficients, the orthorombic elastic matrix has only 9 independent coefficients. If the axes are chosen as indicated in Fig.1.b, the resulting form of the linear compressibility for these phases is :

$$
\begin{aligned}
\chi_{\epsilon} &= (s_{11} + s_{12})\epsilon_1^2 + (s_{12} + s_{22})\epsilon_2^2 + (s_{13} + s_{23})\epsilon_3^2 \\
&+ (s_{15} + s_{25})\epsilon_1\epsilon_3
\end{aligned}
\tag{4}
$$

For orthorombic (untilted) phases the last term vanishes. This formula allows one to predict the value of the linear compressibility in a particular plane. If the plane of the sample is considered, then ϵ can be defined by the azimuth angle ϕ (cf. Fig.1.a), $\epsilon = \cos\phi\, \mathbf{x_1} + \sin\phi\, \mathbf{x_2}$, and :

$$
\chi_{\epsilon} = (s_{11} + s_{12})\cos^2\phi + (s_{12} + s_{22})\sin^2\phi
\tag{5}
$$

For monoclinic phases, where the molecules are tilted from the vertical by an angle θ, another interesting plane to consider is the one perpendicular to the molecular axis (that we will call the transverse plane). In that plane we have $\epsilon = (\cos\phi/\cos\theta)\, \mathbf{x_1} + \sin\phi\, \mathbf{x_2} - \tan\theta\cos\phi\, \mathbf{x_3}$ (the azimuth ϕ is indicated Fig.1.b), and :

$$
\begin{aligned}
\chi_{\epsilon} &= [(s_{11} + s_{12}) - (s_{15} + s_{25})\sin\theta \\
&\qquad + (s_{13} + s_{23})\sin^2\theta]/\cos^2\theta \times \cos^2\phi \\
&+ (s_{12} + s_{22})\sin^2\phi
\end{aligned}
\tag{6}
$$

This shows that if one is able to measure two linear compressibilities in the plane of the sample, this is sufficient to yield all the linear compressibilities in that plane, and to determine the coefficients

$(s_{11}+s_{12})$ and $(s_{12}+s_{22})$. If the molecular tilt θ can be measured independently, two linear compressibilities in the transverse plane can be evaluated, hence all the linear compressibilities in that plane. One has therefore access to the coefficient $[(s_{11}+s_{12})-(s_{15}+s_{25})\sin\theta+(s_{13}+s_{23})\sin^2\theta]/\cos^2\theta$. If one is able to evaluate this coefficient in a large enough tilt angle range, then $(s_{13}+s_{23})$ and $(s_{15}+s_{25})$ can be obtained.

The two diffraction peaks generally found in GID experiments for orthorombic or monoclinic phases allow one to measure two such linear compressibilities in the plane of the sample, and the tilt angle can be determined from the Bragg-rod profiles. It is then, in principle, possible to have access to all these combinations of coefficients.

3   Experimental Technique

The grazing incidence diffraction (GID) experiments were carried out at the D41B beamline of the LURE-DCI storage ring in Orsay, France. The $\lambda = 0.1488nm$ radiation was selected using a $Ge(111)$ monochromator. The grazing angle of incidence $\theta_i = 2.09mrad$ was fixed slightly below the critical angle for total external reflection using a mirror. The width and height of the incident beam were fixed by slits. The diffracted radiation with in-plane wave-vector transfer q_{xy} was selected using a Soller collimator (opening $1.43mrad$, i.e. $0.0056\mathring{A}^{-1}$ at $1.5\mathring{A}^{-1}$), and detected in a vertically mounted argon-filled position sensitive detector (PSD)[17].

The Langmuir trough mounted on the diffractometer was equipped with a movable single barrier, allowing the compression of the film. The surface pressure Π was measured using a Whilhelmy balance. The vessel containing the trough was sealed, pumped and filled with a flow of water saturated helium. The temperature was regulated to within $\pm 0.5°C$ using the water of a large thermal bath.

The amphiphilic molecules used where fatty acids $C_{n-1}H_{2n-1}COOH$, purchased from Fluka ($> 99\%$ purity), and used as obtained. Two different chain lengths were investigated: behenic acid $n = 22$ (we shall sometimes use C_{22} for it in the following), and myristic acid $n = 14$ (C_{14}) in order to get a first insight into the role of chain length (for a simple homogeneous solid plate the compressibility is expected to be proportional to the thickness). Behenic acid was dissolved in

chloroform and myristic acid in hexane (both from Merck, analytical grade), to a concentration of $1g/l$, and approximately $100\mu l$ of the solution was carefully spread on the water surface.

The film was then compressed step-by-step, and Bragg peaks were recorded at each (fixed) pressure step. The total time required to record the Bragg peaks and Bragg rods was typically 3 hours per step.

4   Results

4.1   Characterization of the unit-cell parameters

All the crystals investigated in this study have a two-dimensional rectangular (distorted hexagonal) unit-cell (Fig.1). In the L_2 (smectic I according to the liquid crystal terminology) and L_2'' (smectic I') phases, molecules are tilted towards one of their six nearest neighbors, whereas in the L_2' (smectic F) phase they are tilted towards one of their six next-nearest neighbours. In the more ordered S (smectic U') and CS (smectic U) phases, there is no molecular tilt. Phase diagrams of behenic and myristic acids can respectively be found in references [5, 6] and [18, 19].

The peak positions measured in the horizontal plane for the two different fatty acids at different temperatures are given Fig.2 and 3, where the corresponding phases are indicated.

For all these phases, only the two lowest-order diffraction peaks are observed, corresponding to the {1,1} (degenerate) and {2,0} (non-degenerate) Bragg reflections (cf Fig.4). The d spacing of the corresponding diffracting planes can be very simply derived from the powder-diffraction peak position q_{xy} (obtained as well as the hwhm by fitting the peak with a Lorentzian) by: $d = 2\pi/q_{xy}$. Both cell parameters a and b, characterizing the size of the rectangular cell in the horizontal plane, are hence precisely determined from the diffraction data. The molecular area is then given by $A = ab/2$.

The tilt angle can be extracted from the rod-scans in the following way. The maximum intensity in the Bragg rod is obtained when the wave-vector transfer $\mathbf{q}$ is perpendicular to the molecular axis, whose direction is given by the director $\mathbf{n}$. From the relation $\mathbf{q}.\mathbf{n} = \mathbf{0}$ we get: $q_z = q_{xy}\tan\theta\,\cos\psi$ where ψ is the azimuthal angle between the projections of $\mathbf{q}$ and $\mathbf{n}$ in the horizontal plane. Hence

the $\{1,1\}$ peak, for which ψ is never equal to $\pi/2$, has a non-zero q_z component in all tilted phases (L_2, L_2', L_2''). On the other hand, the $\{2,0\}$ peak has a non-zero q_z component only in the L_2' phase ($\psi = 0$), since $\psi = \pi/2$ in the L_2 and L_2'' phases. The value of q_z, which can be obtained from the rod-scans, coupled to the knowledge of the tilt direction (which can itself be deduced from the number of peaks having a q_z component), leads to the value of the tilt angle.

The cell parameters and tilt angle deduced from the peaks positions are given Fig.5 for C_{22} and Fig.6 for C_{14}.

4.2   Peak widths and range of the positional order

Phases might be classed according to their cristallization direction(s) [20]. Some of them (the lower temperature phases : CS and L_2'') are supposed to be 2D crystals, with long-range positional order in two directions. Other intermediate phases (S, L_2' and L_{2h}) should have long-range order in one direction (perpendicular to the tilt direction for tilted phases), but not in the other. Finally hexatic phases (L_{2d}) obtained for higher temperature have no long-range positional order at all.

The most straightforward way to track long-range positional order is to consider the Bragg peak widths, inversely proportional to the correlation length of the diffracting planes. The half width at half maximum of the peaks are plotted in Fig.7. The situation appears to be different for the L_2'' and CS phases (lower inset): whereas CS has two resolution-limited peaks, supporting the fact that it is, indeed, a 2D crystal, L_2'' has one resolution-limited peak, and one very narrow but not resolution limited peak, possibly implying that cristallization along a (parallel to the molecular tilt) is not perfect. The anisotropy in correlation lengths of the intermediate phases (middle inset) appears clearly with L_{2h} phase, whose two peaks have very different widths. As for L_2'' phase though, the expected cristallization (along b this time) is not perfect, since the corresponding $\{2,0\}$ peak is not quite resolution-limited. In the L_2'' and S phases, the anisotropy of cristallization is difficult to determine, since both peaks correspond to Bragg planes in directions with no long-range order, and are consequently broad. The increase in correlation length can although be noticed, when passing from L_2' to S. The hexatic phase (L_{2d}, upper inset) has inequally broad peaks, showing that though neither principal direction possess long-range order, one of them (perpendicular to the molecular tilt)

is ordered on a longer scale.

4.3   Isotherms

It is interesting to compare the isotherms obtained by determining the molecular area from the trough area and the quantity of product spread with those derived from the x-ray measured molecular area. This is presented in Fig.8 and Fig.9. One can see that the pressure rises later for microscopically determined areas, owing to the fact that the film is inhomogenous. This point has been stressed in Ref.[6]; the actual (x-ray measured) molecular area is in fact smaller than the assumed molecular area, which takes into account large surfaces deprived of film. However, the molecular areas obtained using the trough area and the spreaded amount are smaller at higher pressure than those determined by using the x-ray derived molecular areas: this is due to the loss of amphiphilic molecules, either in the subphase, through the barriers, or by collapse. For all these reasons, one can see that compressibilities cannot be reliably determined from a standard isotherm, and that only diffraction data can bring reliable results. Also, the diffraction data can give access to the anisotropic linear compressibilities, which is not the case when using the standard isotherms.

For behenic acid at $T = 8°C$, the trough isotherm shows a L'_2 phase that has not been observed with x-rays, possibly because its range of existence is very small.

4.4   Transverse cell

A good way to look at the data, as was pointed out by Kuzmenko et al. [20], is to consider the parameter cells in the transverse plane, and to plot the transverse parameter b_T against the transverse parameter a_T, as illustrated in Fig.10. This way of plotting the data allows one to put emphasis on the kind of molecular packing and will help us to better understand the negative linear compressibilities obtained in the transverse plane (see below).

Phases are distributed on an arc, the extremities of which correspond to densely packed phases (with backbone ordering), and center to less densely packed phases (with no backbone ordering). There are two possible backbone arrangements for carbon chains [20] : herringbone (HB) or pseudo-herringbone (PHB) as shown in Fig.11. Backbone packing strongly influences the size and shape

of the rectangular cell, which is why backbone ordered phases are distributed on either end of the arc, depending on whether they achieve HB or PHB packing. Almost all phases possessing backbone ordering (ie. in our case L_2', L_2'', S and CS) have HB packing. The only known phase with PHB packing is a particular type of the so-called L_2 phase, L_{2h} [20]. The other type L_{2d} possesses no backbone ordering, and in consequence has a quasi hexagonal cell ($b = \sqrt{3}a$), which places it in the middle of the arc. Upon decrease of temperature, the system stays on the arc, passing from its center (undistorted unit-cell, molecules free to rotate around their axis), to one of its ends (molecules with a definite azimuthal position).

The rescaling with chain length of the phase diagram of fatty acids [18] implies that for a same temperature, molecules with shorter chains will organize in less dense phases (i.e. at higher a_T and b_T, placing them more in the center of the arc). This is in complete agreement with our results, which place the L_2 phases of C_{14} almost exactly in the middle of the arc (making them L_{2d} phases, perhaps with a faint PHB ordering), and all the phases of C_{22} towards the extremities. For C_{14}, $4°C$ gives acces to "high temperature phases", whereas for C_{22}, $20°C$ still leads to "low temperature phases".

The first interesting remark about Fig.10 is that for the same temperature, under compression, the transverse cell roughly keeps its area (deplacement along a line where the product $a_T b_T$ is constant), but it jumps from one end of the arc (PHB) to the other (HB) when passing from L_{2h} to L_2' or L_2''. These two particular phase transitions involve a complete rearrangement of the cell around its central molecule, since not only the backbone packing, but also the transverse cell dimensions undergo a discontinuous change (this discontinuity does not exist in the in-plane parameters a and b). This jump is of particular interest to us, since it might explain some unexpected features of the compressibilities we measured, as will be explained below.

The second interesting remark about Fig.10 is that the spread of points of the different phases have very different extensions and directions. This can be related to an anisotropy in transverse compressibility (that will be developed in the next section), and compared with the anisotropy in cristallization. The L_{2d} phases roughly extend in the direction of a "constant geometry" line (for which the ratio b/a stays constant), showing an equivalent compressibility in both the a_T and

b_T direction. The L_{2h} and L_2'' phases extend in a direction of constant b_T, indicating a stronger compressibility along a_T, whereas the L_2' and S phases extend in a direction of constant b_T, related to a larger compressibility along a_T. For the CS phases, the extension of the spread of points on the diagram is almost null.

4.5 Compressibilities

The different compressibilities calculated from our data are given in table 1 for the two different compounds and in the different phases studied. The compressibilities range from 0.1 to $8m/N$, and, surprisingly, three distinct orders of magnitude can be clearly identified: around $6m/N$ for the tilted phases, $0.6m/N$ for the S phase, and $0.2m/N$ for the CS phase.

Because the different phases are anisotropic, it is interesting to discriminate along the different directions in order to better understand this hierarchy of compressibilities. The most interesting linear compressibilities are those along the unit-cell axes a and b with $\chi = \chi_a + \chi_b$, and the anisotropy is best visualized by building polar diagrams representing the magnitude of the linear compressibility along a given direction (i.e. the relative distortion along that direction under an isotropic 2D stress) as a function of the angle that this direction makes with the unit-cell axes. Such polar diagrams can be constructed using the relations 5 and 6 of section 2. They are represented in Fig.12 (with the same scale) for the different phases we investigated. Polar diagrams make it obvious that most phases have a highly anisotropic compressibility. In fact, the only isotropic phase, from the point of view of compressibility is the CS phase. The other extreme is represented by the L_2'' phase for which the linear compressibilities χ_a and χ_b differ by two orders of magnitude. The anisotropy might be traced back either to the anisotropy induced by the tilt direction (in-plane compressibilities of the L_2, L_2' and L_2'' phases), or to the anisotropy induced by 1D cristallization like in the S phase (see also Fig.13). Let us recall to this point that tilted phases have their long-range positional order direction perpendicular to their tilt direction (transverse L_2 compressibilities), and the S phase, perpendicular to the tilt direction of the L_2' phase from which it originated upon compression.
The central result of this paper which summarizes these data is Fig.14, where the linear compress-

ibilities along the a and b axes are represented on a log-log scale. Different regions corresponding to compressibilities presumably associated with different mechanisms can be clearly identified on this figure, where the anisotropy is also most clearly visible. The largest linear compressibilities are observed in the L_2 (right, central), L_2' (central, top) and L_2'' (right, bottom) phases in the tilt direction. The lowest values are observed in some phases and directions where the layer possesses a long range positional order, that is in both direction in the CS phase (left, bottom), in one direction of the S phase (left, central), and in one direction of the L_2'' phase. They have to be related to the compression of already well organized molecular planes. The intermediate values are found in the transverse plane, in one direction of the S phase and of the L_2 and L_2' phases. They correspond to some directions having no long-range positional order (the b direction of S), and others generally expected to have it (the b direction of L_2 and the a direction of L_2').

One can make abstraction of the effect of tilt by looking at the linear compressibilities in the transverse plane normal to the molecular axis. A transverse compressibility $\chi_T = -1/A_T(\partial A_T/\partial \Pi)$, where A_T is the transverse area of the cell, and a tilt compressibility $\chi_\theta = \chi - \chi_T = \tan\theta(\partial\theta/\partial\Pi)$ can then be defined. χ_θ describes the part of the compressibility due to the untilting of the molecules. If the molecules are tilted along a, one can also write $\chi_a = \chi_{a_T} + \chi_\theta$, or $\chi_b = \chi_{b_T} + \chi_\theta$ if they are tilted along b. For the orthorombic phases, the in-plane and transverse compressibilities are of course equal (χ_θ=0). The polar diagram resulting from the linear compressibilities in the transverse plane are represented in Fig.13.

Transverse linear compressibilities are mainly interesting in the tilt direction where they differ from the in-plane compressibilities. In the L_2 phase, linear compressibilities are reduced in the tilt direction from $5m/N$ in the sample plane to $1-2m/N$, i.e. larger but on the order of the intermediate compressibilities mentioned above. More unexpected is that χ_{bT} in the L_2' phase and χ_{aT} in the L_2'' phase are negative.

Finally, it is interesting to note the strong correspondance between linear compressibilities and correlation lengths : The tilted phases only exhibits very short range positional order along the tilt

direction where the compressibility is very large, the CS phase has 2D long-range order, and no noticeable (on the diagram) compressibility in either direction, L_{2h} and S have 1D cristallization, and show larger compressibilities in the direction where they are not cristallized.

5   Discussion

We first summarize the theory of elasticity of thin plates as a basis for the discussion. The four different sets of compressibilities (large compressibilities in the tilted phases, intermediate compressibilities along the direction without tilt nor true long-range order, low compressibilities in the crystal phases, and negative linear compressibilities in the transverse plane) will then be discussed with the aim of assigning a molecular mechanism to each of them.

The central result of the theory of elasticity for thin plates [16] is that the compressibility is proportional to the plate thickness h: $\chi = Eh/(1 - \sigma_p^2)$ where E is the Young modulus and σ_p the Poisson ratio. Of course this is not necessarily a realistic model, but the same trends remain in more realistic approaches: If one is only interested in the interactions between the chains (which up to now are believed to be the relevant part of the amphiphilic molecules), three essential contributions to the film free energy must be considered[21]: attractive van der Waals forces which ensure the film cohesion, the entropy of conformation defects and their energy (which must be included to account for phase transitions). It turns out that all these components roughly scale proportionally to n [21], the number of segments, and it will therefore also be the case for the compressibility which is the second derivative of the free energy with respect to the area.

5.1   Compressibility of the tilted phases

The compressibilities of the tilted phases are the largest that we observe ($> 5m/N$, see table 1). The expectation that the compressibilities should scale with the segment number (i.e. a factor of 1.7 between myristic and behenic acid) is in strong contrast with our experimental observation that the

compressibilities of behenic acid and myristic acid in the L_2 phase at $8°C$ are identical. Indeed all our results tend to indicate that the compressibility of tilted phases are remarkably independent of chain length (and also of film thickness since the compressibilities do not depend on the tilt angle). This, and other experimental observations detailed below, leads us to propose a reconsideration of the respective roles of aliphatic tails and headgroups in the physics of amphiphilic films. In particular we propose here that the compressibility of tilted phases could be due to the elasticity of the hydrogen-bounded headgroup network. That would also explain the puzzling observation that the compressibilities of behenic acid in the L_2'' and myristic acid in the L_2 phase at $5°C$ are equal (and significantly different from their values at $8°C$).

Further evidence that the role of headgroups needs to be reconsidered is as follows:
Firstly, the so-called "universality" of the phase diagrams is only relevant for molecules having different chain lengths but the same headgroup. As soon as different headgroups are considered like alcohols or esters, significant differences appear in the phase diagram topology [22]. Also striking is the fact that in some cases very high pressures can be achieved with molecules that remain tilted throughout the whole phase diagram, which cannot be understood if the chains only are relevant[23].

Secondly, the data of Fig.15 add very interesting evidence to this interpretation.
Whereas at a given surface pressure, the molecular areas of behenic acid and myristic acid are very similar, as one would expect if the interactions between headgroups are dominant and fix the area, this is not the case for the transverse area which differ by more than $1\mathring{A}^2$: We measured 18.75 and $19.25\mathring{A}^2/molecule$ at respectively $8°C$ and $20°C$ for behenic acid and 20.0 and $20.5\mathring{A}^2/molecule$ at $5°C$ and $8°C$ for myristic acid. (Note that the reduction in molecular area is roughly $0.5A^2/molecule$ when the temperature is decreased by $12°C$, or about $1.75\mathring{A}^2/molecule$ when the chain length is increased by 8 segments, hence leading to the equivalence $1\ CH_2 \equiv 5.25°C$ in good agreement with what is obtained from the transition temperatures in ref.[18], around 5 to $10°C$ per CH_2 group.) Moreover the tilt angle is larger for behenic acid than for myristic acid at the same pressure in the L_2 phase (on the order of $20-25°$ for myristic acid and of $25-35°$ behenic acid).

If the molecular area is mainly to be fixed by the headgroup interactions, one does expect the same molecular area whatever the chain length as is observed, and the differences in cross-section and tilt angle can be understood as follows: Because the van der Waals interactions are stronger between C_{22} chains than between C_{14} chains due to their larger length, the number of defects is smaller and their cross-section is also smaller (i.e. the transverse area as experimentally observed). It is therefore necessary to have a larger tilt angle to achieve the projected area than for shorter, more disordered chains with a larger cross-section.

Finally, the temperature dependance of the compressibilities of the tilted phases presents interesting features. Whereas the compressibility of behenic acid in the L_2 phase only slightly decreases from 20° to 8°, the compressibility of myristic acid significantly increases between 8° and 5° from $5m/N$ to $8m/N$ (the same happens for behenic acid but the phase at 5° is now L_2''). The same increase is reported in Ref.[6] for the L_2 and L_2' phases of behenic acid. This could be related to the anomalous properties of water near 4° due to the hydrogen bound network.

5.2   Intermediate compressibilities

The intermediate compressibilities obtained in the L_2, L_2', L_2'' and S phases along the directions where there is neither tilt nor long range order are on the order of $0.5m/N$. It has been proposed on the basis of a Landau theory of weak crystallization in Ref.[7, 8, 20] that the absence of true long range order could be related to the imperfect ordering of the backbone planes. The compressibility would then be due to the ordering of the molecule positions. An order of magnitude of the corresponding energy can be obtained from our data by comparing the compressibilities of the S phase and CS phase along b, since they both have the same cell geometry and packing (HB), but the S phase has true long-range order only along a, whereas the CS phase is a 2-D crystal. If one assumes that the energy δE necessary to squeeze out the defects is equal to the elastic energy necessary reduce the cell parameter b from its large value in the S phase to its low value in the CS phase, then $\delta E = \delta b^2/\chi_b$, using a simple spring model. δb is the variation of the $b/2$ parameter of the cell, that goes from (7.6/2) to (7.4/2)$\mathring{A}$ for one molecule during the transition. This variation is representative

of the transition from a disordered state to a crystallized state in the b-direction. χ_b is the linear compressibility along b in the S phase $\approx 0.5 m/N$. With these numbers, one obtains $\delta E \approx 2 \times 10^{-22} J$, to be compared to the the thermal energy $k_B T = 4.1 \times 10^{-21} J$, indicating that defects are rather rare, which is consistent with a coherence length of ≈ 30 interatomic distances in the ill-crystallized direction of the S phase.

5.3   Compressibility of crystal phases

The lowest compressibilities where obtained in the CS phase and along the "well crystallized" directions b in the L_2'' phase and a in the S phase. They are on the order or smaller than $0.1 m/N$. It is interesting to compare these values to those obtained for 3D polymer crystals, in particular for orthorombic polyethylene which has a structure similar to that of the CS phase. The values of the linear compressibilities for orthorombic polyethylene reported in Ref.[14] are $1.8 \times 10^{-10} m^2/N$ along a and $1.4 \times 10^{-10} m^2/N$ along b. Let us note that the 2D pressure Π is homogenous to N/m and not N/m^2, which will cause our elastic coefficients to be in m/N. To be compared to the elastic coefficients of similar 3D materials, the bidimensional compressibilities will have to be multiplied by the thickness of the layer (here $2.4 nm$). We obtain $\approx (2.4 \pm 0.3) \times 10^{-10} m^2/N$ along a or b in quite good agreement with the values for polyethylene. The fact that the compressibility of a film is slightly larger than that of a 3D crystal can probably be explained by a larger number of defects. In any case, the compressibility of the 3D polyethylene crystals could be nicely estimated by using only a pairwise intermolecular potential including a short range repulsive exponential potential and long range attractive van der Waals forces for a perfect crystal order with no defects, and one confidently assign the same molecular origin to the lowest compressibilities of fatty acids, i.e. repulsive interactions between methyl groups in a well crystallized solid.

5.4   Negative transverse linear compressibilities

Negative transverse linear compressibilities are only observed in the L_2' and L_2'' tilted phases. We propose an explanation for the negative linear compressibilities on the basis of the transition between PHB and HB packing as follows: Looking at Fig.16, one can see that the transition from L_2 to L_2'

or L_2'' implies a dramatic change in the transverse cell parameters (this can also be seen in Fig.10). In each case one of the transverse parameters (b_T for L_2/L_2' and a_T for L_2/L_2'') increases instead of decreasing upon compression. They happen to be exactly the same for which the negative transverse linear compressibilities are observed upon further compression. It is therefore likely that upon further compression after the PHB to HB transition the unit cell is still reorganizing in the transverse plane towards a preferred geometry, implying negative linear compressibilities.

An important consequence is that the second mechanism presented in Fig.16 (along the diagonal) for the transition from L_2 to L_2', corresponding to a 90° change of the tilt direction, is ruled out, since it would involve a negative compressibility along a_T in the L_2' phase, and not along b_T. This result was already suggested by Brewster Angle Microscopy [24].

6   Conclusion

The linear compressibility of a two-dimensional fatty acid crystal has been measured for the first time. Surprisingly, the linear compressibilities can be nicely divided in 4 sets depending on their value which is characteristic of the phase and direction of crystallization, and a different molecular mechanism could be ascribed to each set. This lead us in particular to propose to reconsider the role of headgroups.

The largest compressibilities (10 m/N) are observed in the tilted phases. They are apparently independant on the chain length and could be related to the reorganization of the headgroup hydrogen-bounded network. The intermediate compressibilities observed in the directions normal to the molecular tilt in the L_2 or L_2' phases and in the S phase in the direction without true long range order could be related to the progressive squeezing of defects in those phases. The lowest compressibilities observed in the solid untilted CS phase and for one direction of the S and L_2'' phases are similar to the compressibilities of crystalline polymers. They correspond to the interactions between methyl groups in the crystal. Finally, the negative compressibilities observed in the transverse plane for the L_2' and L_2'' and can be traced back to subtle reorganizations upon untilting.

Work is in progress in order to solve some remaining puzzling questions:

Is it possible to further demonstrate that the compressibility of tilted phases is mainly due to inter-

actions between headgroups by measuring the compressibility for different headgroups and observing large variations?

Does compressibility really decrease with increasing temperature in those phases and what is the underlying mechanism?

What is the dependence of the compressibility on film thickness (i.e. chain length) in the untilted phases?

Answering those questions would allow a better understanding of the compressibility of two-dimensional Langmuir film crystals and open the way for a more quantitative theoretical approach.

* Laboratoire de Physico-Chimie Curie is UMR 168 associated to the Centre National de la Recherche Scientifique.

References

[1] A. Renault, J.F. Legrand, C. Zakri, J.P. Rieu, F. Graner, B. Berge and G. Grübel, in "Short and Long Chains at Interfaces.", J. Daillant, P. Guenoun, C. Marques, P. Muller, J. Tran Thanh Van Ed., Editions Frontières (Gif-sur-Yvette), p. 219 (1995).

[2] B. Berge, O. Konovalov, J. Lajzerowicz, A. Renault, J.P. Rieu, M. Vallade, J. Als-Nielsen, G. Grübel, and J.F. Legrand, *Phys. Rev. Lett.* **73** 1652 (1994).

[3] S.W. Barton, B.N. Thomas, E.B. Flom, S.A. Rice, B. Lin, J.B. Peng, J.B. Ketterson and P. Dutta, *J. Chem. Phys.* **89** 2257 (1988).

[4] B. Lin, M.C. Shih, T.M. Bohanon, G.E. Ice, and P. Dutta, *Phys. Rev. Lett.* **65** 191 (1990).

[5] R.M. Kenn, C. Böhm, A.M. Bibo, I.R. Peterson, H. Möhwald, J. Als-Nielsen, K. Kjaer, *J. Phys. Chem.* **95** 2092 (1991).

[6] G.M. Bommarito, W.J. Foster, P.S. Pershan, M.L. Schlossman, *J. Chem. Phys.* **105** 5265 (1996).

[7] V.M. Kaganer and E.B. Loginov, *Phys. Rev. Lett.* **71** 2599 (1993).

[8] V.M. Kaganer, I.R. Peterson, R.M. Kenn, M.C. Shih, M. Durbin, P. Dutta, *J. Chem. Phys.* **102** 9412 (1995).

[9] S. Karaborni in "Short and Long Chains at Interfaces.", J. Daillant, P. Guenoun, C. Marques, P. Muller, J. Tran Thanh Van Ed., Editions Frontières (Gif-sur-Yvette), p. 113 (1995), and references therein.

[10] F.M. Haas and R. Hilfer, *J. Chem. Phys.* **105** 3859 (1996).

[11] B.M. Abraham, K. Miyano, J.B. Ketterson, and S.Q. Xu, *J. Chem. Phys.* **78** 4776 (1983); B.M. Abraham, K. Miyano, J.B. Ketterson, and S.Q. Xu, *Phys. Rev. Lett.* **51** 1975 (1983).

[12] H. Bercegol and J. Meunier, *Nature* **356** 226 (1992).

[13] A. Saint-Jalmes, M. Assenheimer and F. Gallet, submitted to *Phys. Rev. Lett.*.

[14] K. Tashiro, M. Kobayashi, H. Tadokoro, Macromolecules, **11**(5), 914 (1978)

[15] J.F. Nye, "Physical Properties of Crystals", Clarendon Press, Oxford.

[16] L. Landau and E. Lifschitz, "Theory of Elasticity", $3^r d$ edition, Pergamon Press, New-York, 1959, p.7.

[17] Designed and built by the detector group at LURE.

[18] A.M. Bibo and I.R. Peterson, Adv. Mater. **2**, 309 (1990)

[19] S. Akamatsu and F. Rondelez, *J. Phys. II France* **1** 1309 (1991).

[20] I. Kuzmenko, V.M. Kaganer, and L. Leiserowitz, preprint (11 July 1997).

[21] J.P. Rieu and M. Vallade, *J. Chem. Phys.* 104 7729 (1996).

[22] B. Fischer, E. Teer, and C.M. Knobler, *J. Chem. Phys.* **103** 2365 (1995); E. Teer, C.M. Knobler, C. Lautz, S. Wurlitzer, J. Kildae, and T.M. Fischer, *J. Chem. Phys.* **106** 1913 (1997).

[23] F. Graner, S. Perez-Oyarzun, A. Saint-Jalmes, C. Flament, and F. Gallet, *J. Phys. II France* **5** 313 (1995).

[24] S. Rivière, S. Hénon, J. Meunier, D.K. Schwartz, M.V. Tsao, and C.M. Knobler, *J. Chem. Phys.* **101** 10045 (1994)

	Behenic acid (C22)			Myristic acid (C14)	
	20^oC	8^oC	5^oC	8^oC	5^oC
L_2	$\chi = \mathbf{6.02 \pm 0.21}$ $\chi_a = 5.45 \pm 0.28$ $\chi_{a_T} = 1.02 \pm 0.17$ $\chi_b = 0.57 \pm 0.04$	$\chi = \mathbf{5.04 \pm 0.06}$ $\chi_a = 4.55 \pm 0.13$ $\chi_{a_T} = 1.94 \pm 0.44$ $\chi_b = 0.52 \pm 0.07$		$\chi = \mathbf{5.05 \pm 0.26}$ $\chi_a = 4.54 \pm 0.29$ $\chi_{a_T} = 1.63 \pm 0.63$ $\chi_b = 0.61 \pm 0.06$	$\chi = \mathbf{7.80 \pm 0.51}$ $\chi_a = 6.97 \pm 0.47$ $\chi_{a_T} = 1.19 \pm 0.65$ $\chi_b = 0.67 \pm 0.07$
L_2'	$\chi = \mathbf{5.04 \pm ...}$ $\chi_a = 0.544 \pm ...$ $\chi_b = 4.597 \pm ...$ $\chi_{b_T} = -1.30 \pm 0.84$				
L_2''			$\chi = \mathbf{7.52 \pm 0.33}$ $\chi_a = 7.46 \pm 0.33$ $\chi_b = 0.082 \pm 0.026$ $\chi_{a_T} = -0.72 \pm 0.52$		
S	$\chi = \mathbf{0.565 \pm 0.209}$ $\chi_a = 0.114 \pm 0.178$ $\chi_b = 0.496 \pm 0.261$				
CS		$\chi = \mathbf{0.209 \pm 0.013}$ $\chi_a = 0.107 \pm 0.010$ $\chi_b = 0.103 \pm 0.006$	$\chi = \mathbf{0.151 \pm 0.296}$ $\chi_a = 0.110 \pm 0.130$ $\chi_b = 0.092 \pm 0.120$		

Table 1: Compressibilities (bold font), linear compressibilities and transverse compressibilities in the L_2, L_2', L_2'', S, and CS phases for behenic acid at 5°C, 8°C, and 20°C and myristic acid at at 5°C and 8°C in m/N.

Figure 1: Unit-cell geometry for an orthorombic phase (a) and a monoclinic phase (b). The molecular tilt in (b) is towards the nearest neighbors (NN) as in the L_2 or L_2'' phases. ϕ is the azimuth angle defining the direction ϵ in the monolayer plane in (a) and in the transverse plane normal to the molecular tilt in (b).

Figure 2: Bragg peak positions for behenic acid at three different temperatures $5°C$, $8°C$, and $20°C$ as a function of surface pressure. The filled squares indicate the position of the non-degenerate $\{2,0\}$ peak, while the empty circles indicate the position of the degenerate $\{1,1\}$ peak.

Figure 3: Bragg peak positions for myristic acid at two different temperatures $5°C$ and $8°C$ as a function of surface pressure. The filled squares indicate the position of the non-degenerate $\{2,0\}$ peak, while the empty circles indicate the position of the degenerate $\{1,1\}$ peak.

Figure 4: Unit-cell and kinematics of in-plane diffraction from tilted phases. Dark grey triangles are for a molecular tilt towards nearest neighbors (NN) and light grey triangles for a molecular tilt towards next nearest neighbors (NNN). The Bragg planes are indicated as broken lines.

Figure 5: Molecular tilt and unit-cell parameters for behenic acid at three different temperatures $5°C$ (empty grey squares), $8°C$ (empty black circles), and $20°C$ (filled black squares) as a function of surface pressure. The dashed lines separating the different phase regions are only a guide for the eye.

Figure 6: Molecular tilt and unit-cell parameters for myristic acid at two different temperatures $5°C$ (grey squares) and $8°C$ (black circles) as a function of surface pressure.

Figure 7: Bragg peak widths in the different phases as a function of surface pressure. The filled symbols indicate the position of the non-degenerate $\{2,0\}$ peak, while the empty symbols indicate the position of the degenerate $\{1,1\}$ peak. Top: Myristic acid at $5°C$ (squares) and $8°C$ (circles); Middle: Behenic acid at $8°C$ (squares) and $20°C$ (circles); Bottom: Behenic acid at $5°$.

Figure 8: Molecular area vs surface pressure isotherms for behenic acid at three different temperatures $5°C$ (empty light grey diamonds and light grey line), $8°C$ (empty grey circles and grey line), and $20°C$ (filled black squares and black line). The molecular area was determined from x-ray measurements (points) or from spreaded amount and trough area (continuous lines).

Figure 9: Molecular area vs surface pressure isotherms for myristic acid at two different temperatures $5°C$ (empty grey diamonds and grey line) and $8°C$ (empty black circles and black line), The molecular area was determined from x-ray measurements (points) or from spreaded amount and trough area (continuous lines).

Figure 10: Distribution of the different phases as a function of their transverse cell parameters: L_2 (empty circles), L_2' (filled squares), L_2'' (inverted triangles), S (empty diamonds), and CS (empty squares). The solid lines indicate a constant area and the broken lines a constant cell geometry.

Figure 11: The two different types of molecular packing found in fatty acid mesophases. The molecular tilt is schematically suggested by representing a top and bottom methyl group orientated as to indicate the azimuth. The pseudo-herrigbone (PHB) packing is found only in the L_2 phase. All other phases have herringbone (HB) packing.

Figure 12: Polar diagrams of the in-plane linear compressibilities in the L_2 phase of behenic and myristic acids, and the L_2', L_2'', S, and CS phases of behenic acid. Grey lines are used for myristic acid in the L_2 phase. The unit-cell is indicated by broken grey lines and the molecular tilt direction by grey symbols. See also Fig.13 for an enlarged plot of the linear compressibilities of S and CS phases.

Figure 13: Polar diagrams of the transverse linear compressibilities in the L_2 phase of behenic and myristic acids, and the L_2', L_2'', S, and CS phases of behenic acid. Grey lines are used for myristic acid in the L_2 phase and the CS phase of behenic acid. The grey shaded lobes indicate a negative transverse compressibility. The unit-cell is indicated by broken grey lines and the molecular tilt direction by grey symbols.

Figure 14: Distribution of the different phases as a function of their compressibilities along the two principal directions of the cell: L_2 (empty circles), L_2' (inverted triangle), L_2'' (diamond), S (empty square), CS (triangles). The transverse compressibility in the L_2 phase is also represented (filled black circles). The broken line indicates isotropic compressibility ($\chi_a = \chi_b$), whereas the dotted lines roughly separate the different regions of compressibility.

Figure 15: Molecular area (circles) and transverse molecular area (squares and triangles) as a function of surface pressure. Filled symbols are for myristic acid at $5°C$ and $8°C$; empty circles for behenic acid at $8°C$ (squares) and $20°C$. Triangles are for the L_2 phase and inverted triangles for the L_2' phase.

Figure 16: Transverse unit-cell geometries found in the tilted phases L_2 (top left), L_2' (bottom left and right) and L_2'' (top right). The molecular tilt is schematically suggested by representing a top and bottom methyl group orientated as to indicate the azimuth. The unit-cell is represented by solid lines. Note that the scale of the a and b axes has been respected. Dotted lines represent Bragg planes with long range positional order. The L_2 to L_2'' phase transition and to different scenarios for the L_2 to L_2' phase transitions are indicated by arrows and the change in unit-cell parameters is given. In the case of the L_2 to L_2'' phase transition, the scenario with the broken arrow can be ruled-out (see text for details); note that a and b are exchanged during the observed transition.

Figure 17: Schematics of the three suggested molecular mechanisms for (a) the compressibility of the tilted phases where the hydrogen bounded network of headgroups is proposed to play an important role, (b) the linear compressibility along directions of imperfect 1D crystallization where positional defects are important, and (c) the CS phases and directions of perfect 1D crystallization where the compressibility is due to the repulsive interaction between well-crystallized methyl groups.

$\vec{n}$

ϕ

$\vec{\epsilon}$

$\mathbf{x_2}$

$\mathbf{x_1}$

b

a

sample plane

(a)

$\vec{n}$

ϕ

$\vec{\epsilon}$

a_T

transverse plane

θ

b_T

$\mathbf{x_3}$

$\mathbf{x_2}$

θ

$\mathbf{x_1}$

(b)

Fig. 1

25

Fig. 2

Fig. 3

a

b

$2\pi/q_{xy}^{\{2,0\}}$

$2\pi/q_{xy}^{\{1,1\}}$

◀ NN Tilt

△ NNN Tilt

$q_{xy}^{\{2,0\}}$

$q_{xy}^{\{1,1\}}$

ϕ n_{xy}^{NN}

$q_{xy}^{\{1,\bar{1}\}}$

n_{xy}^{NNN}
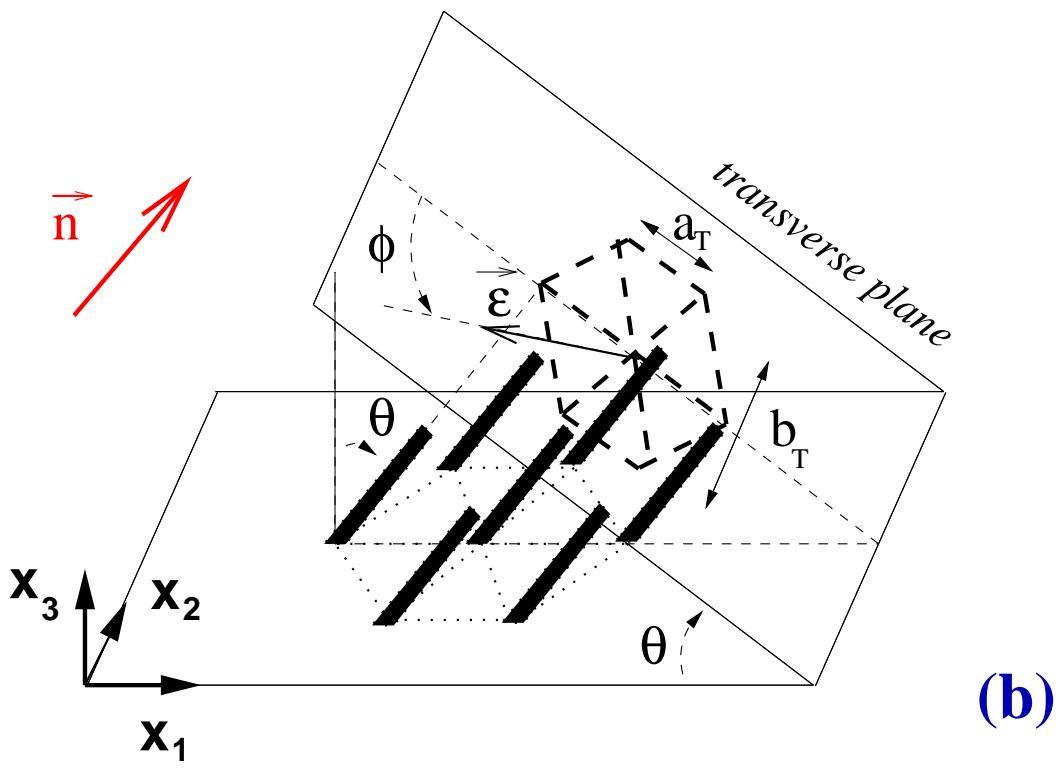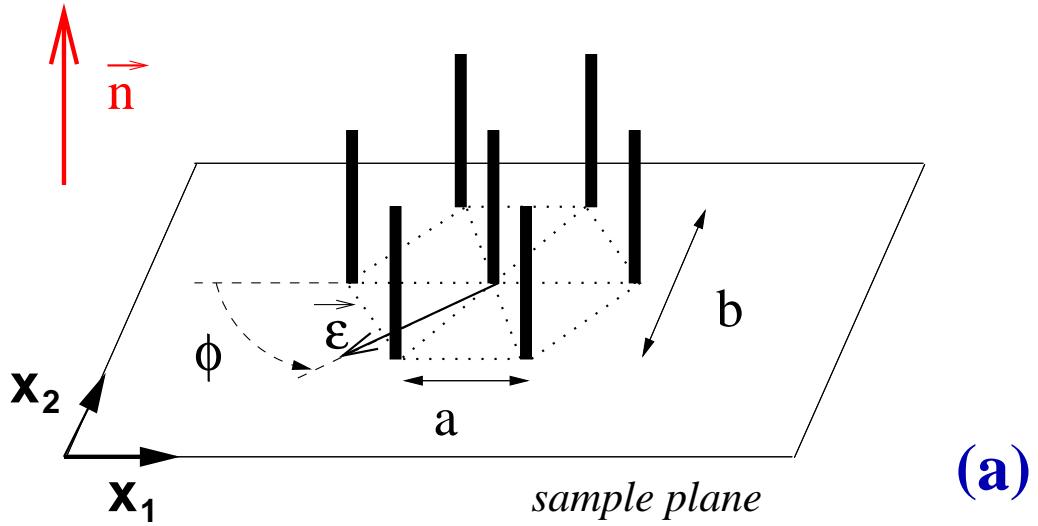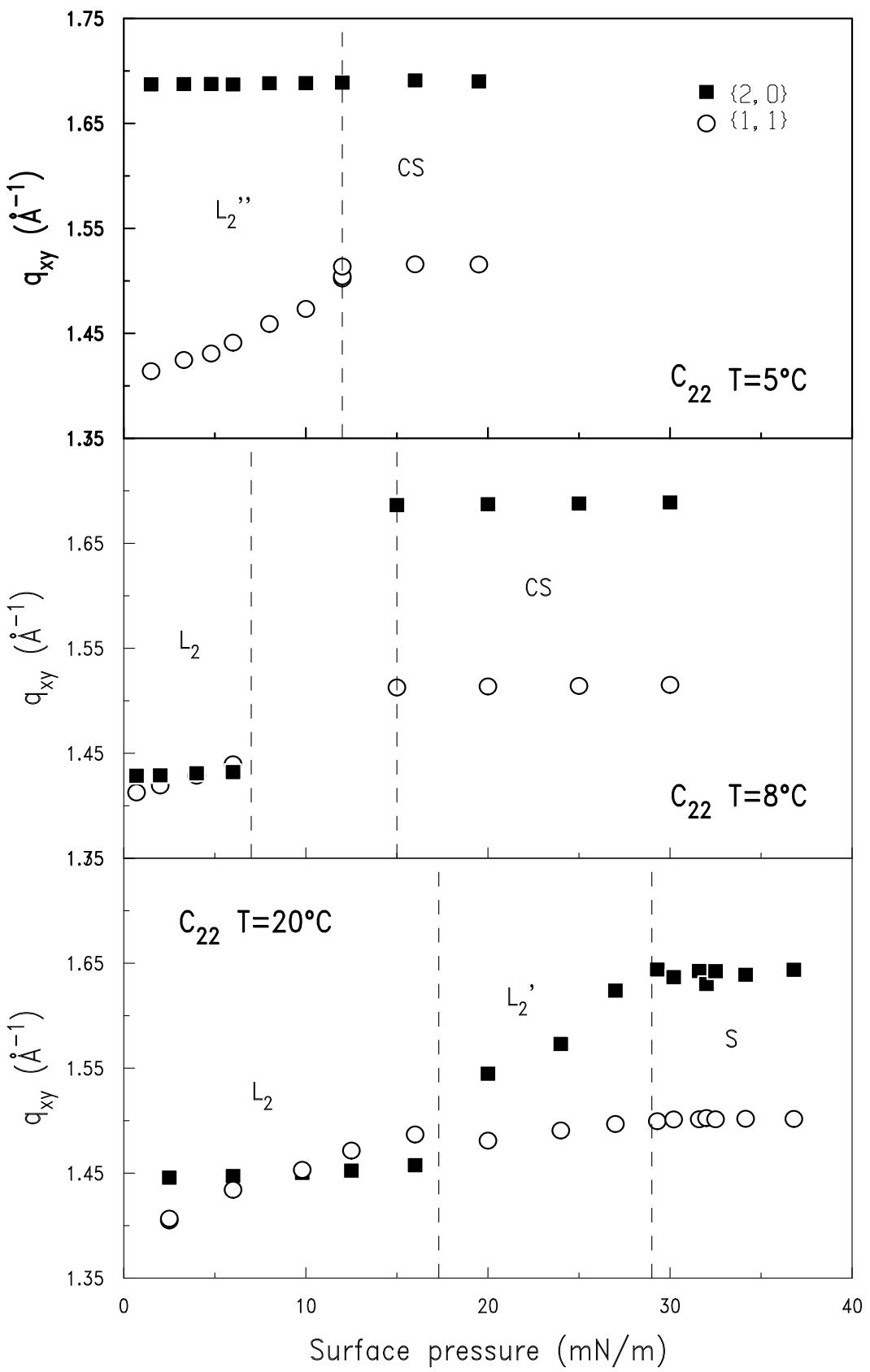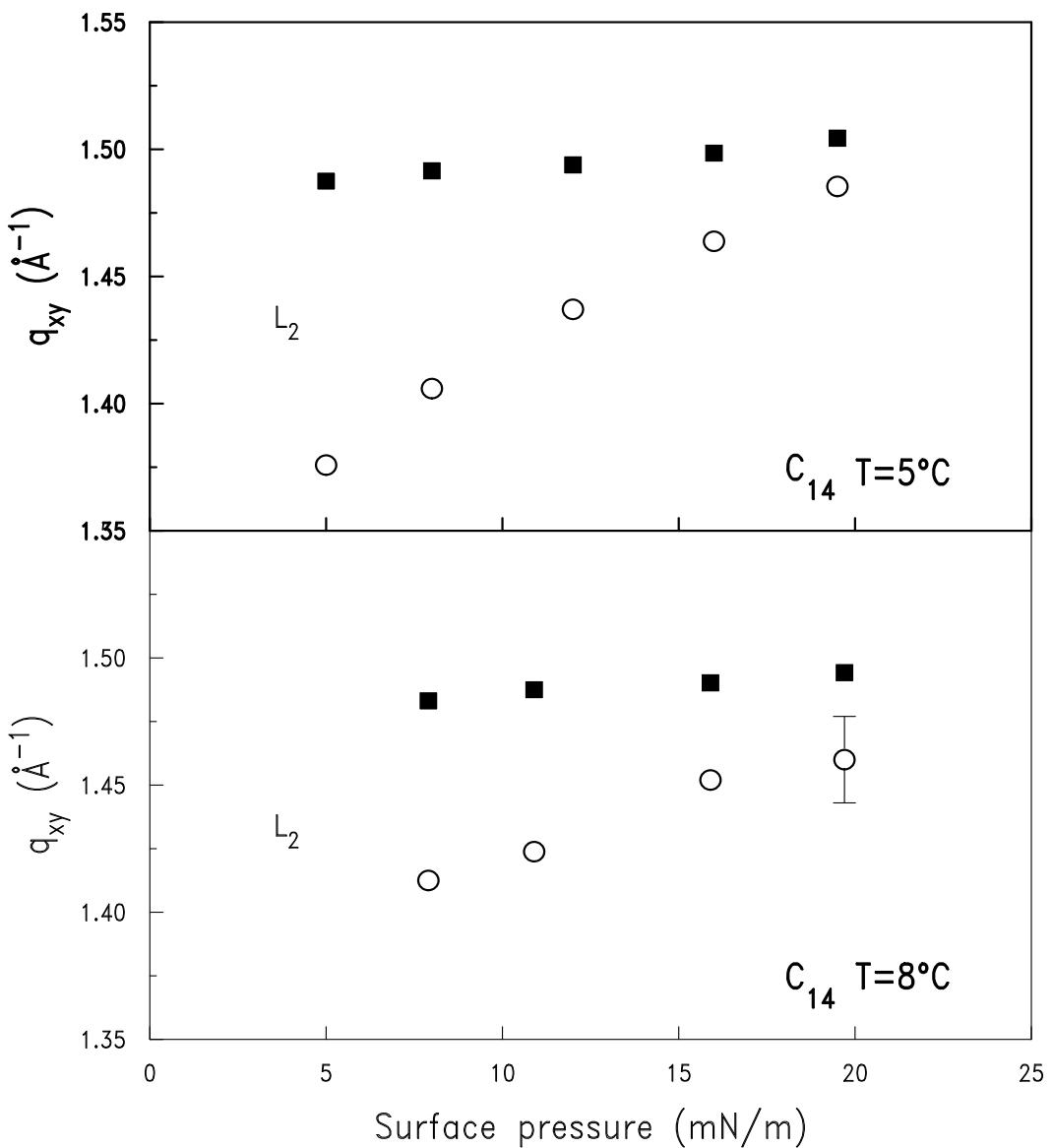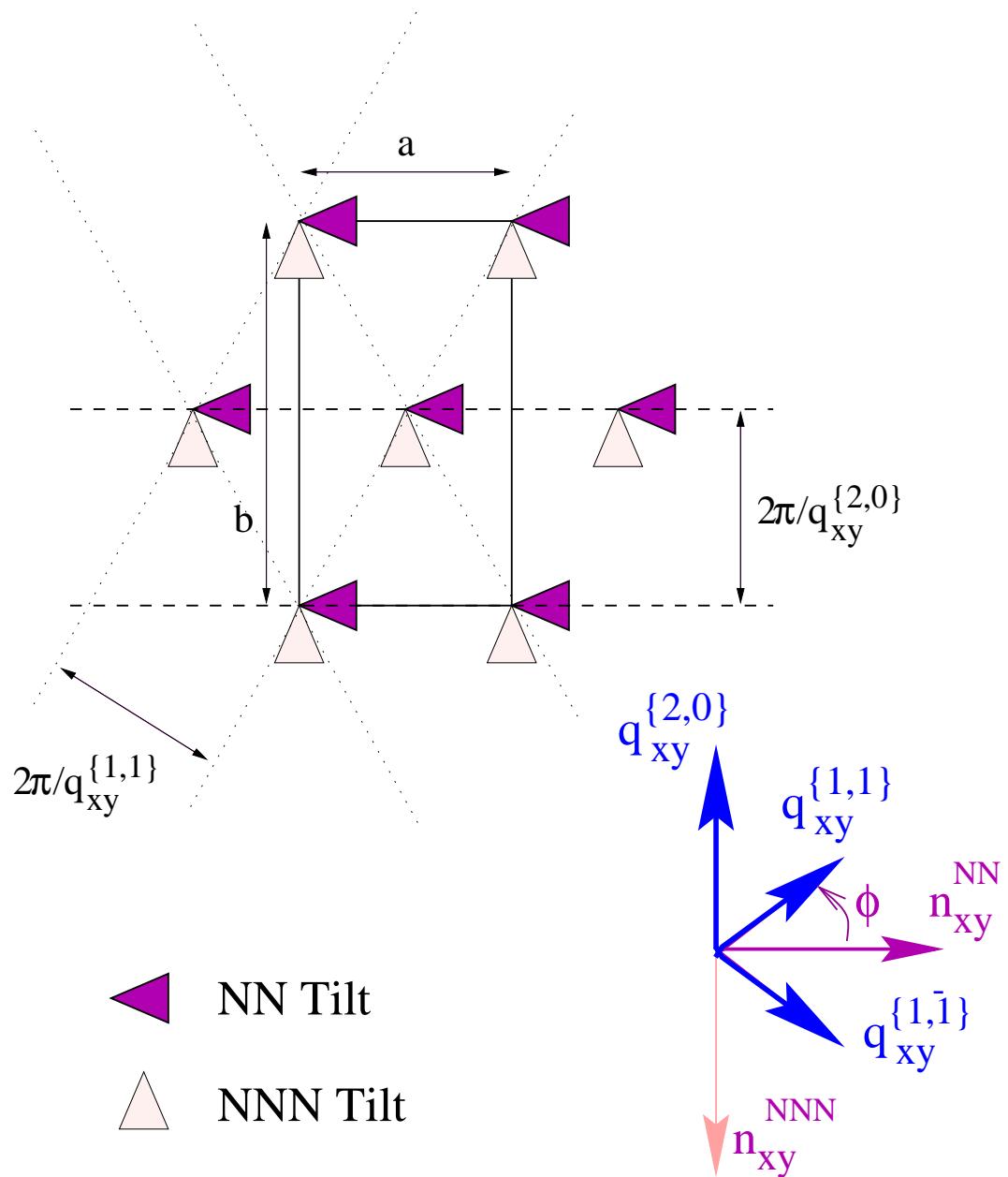
Fig. 4
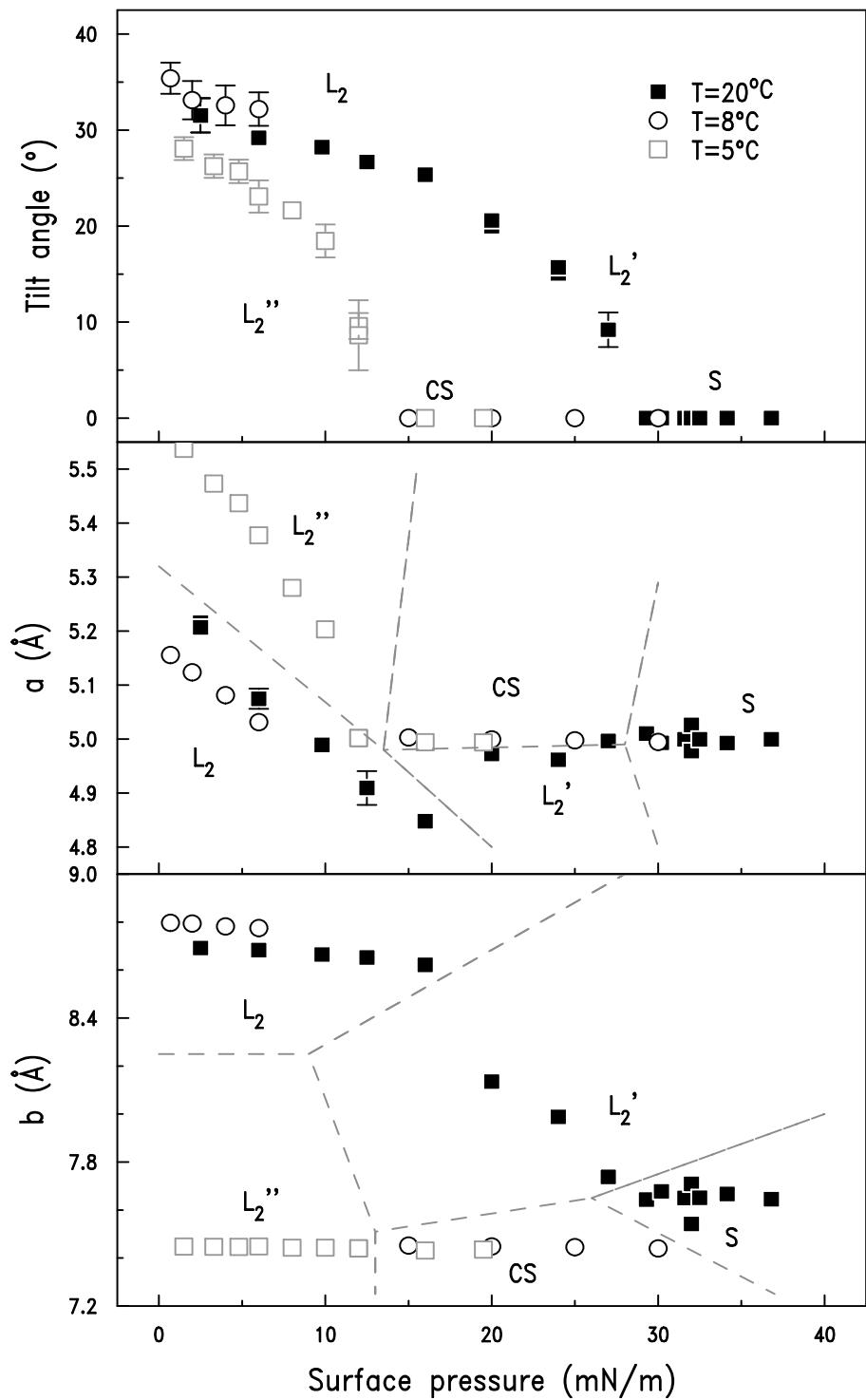
Fig. 5
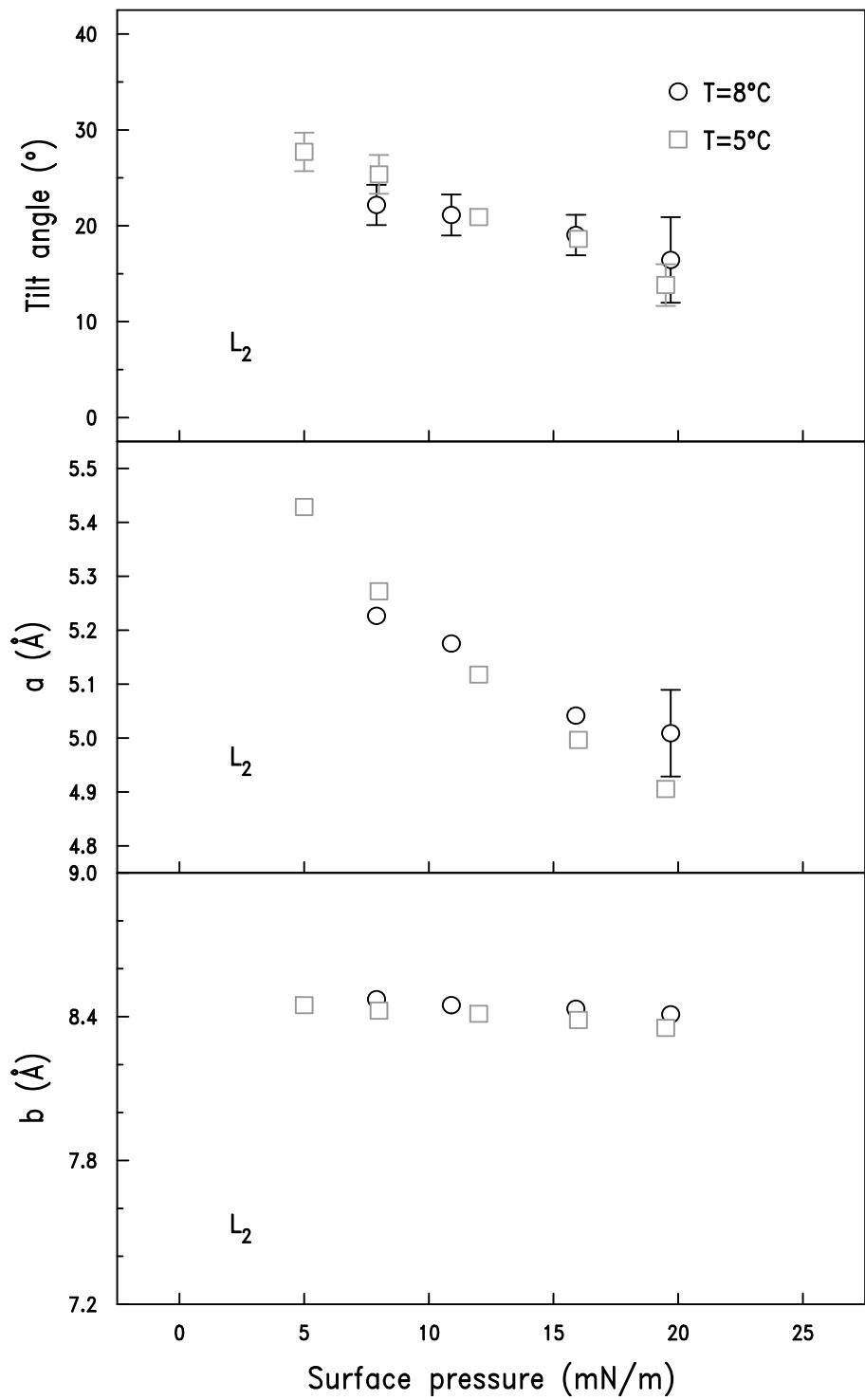
Fig. 6
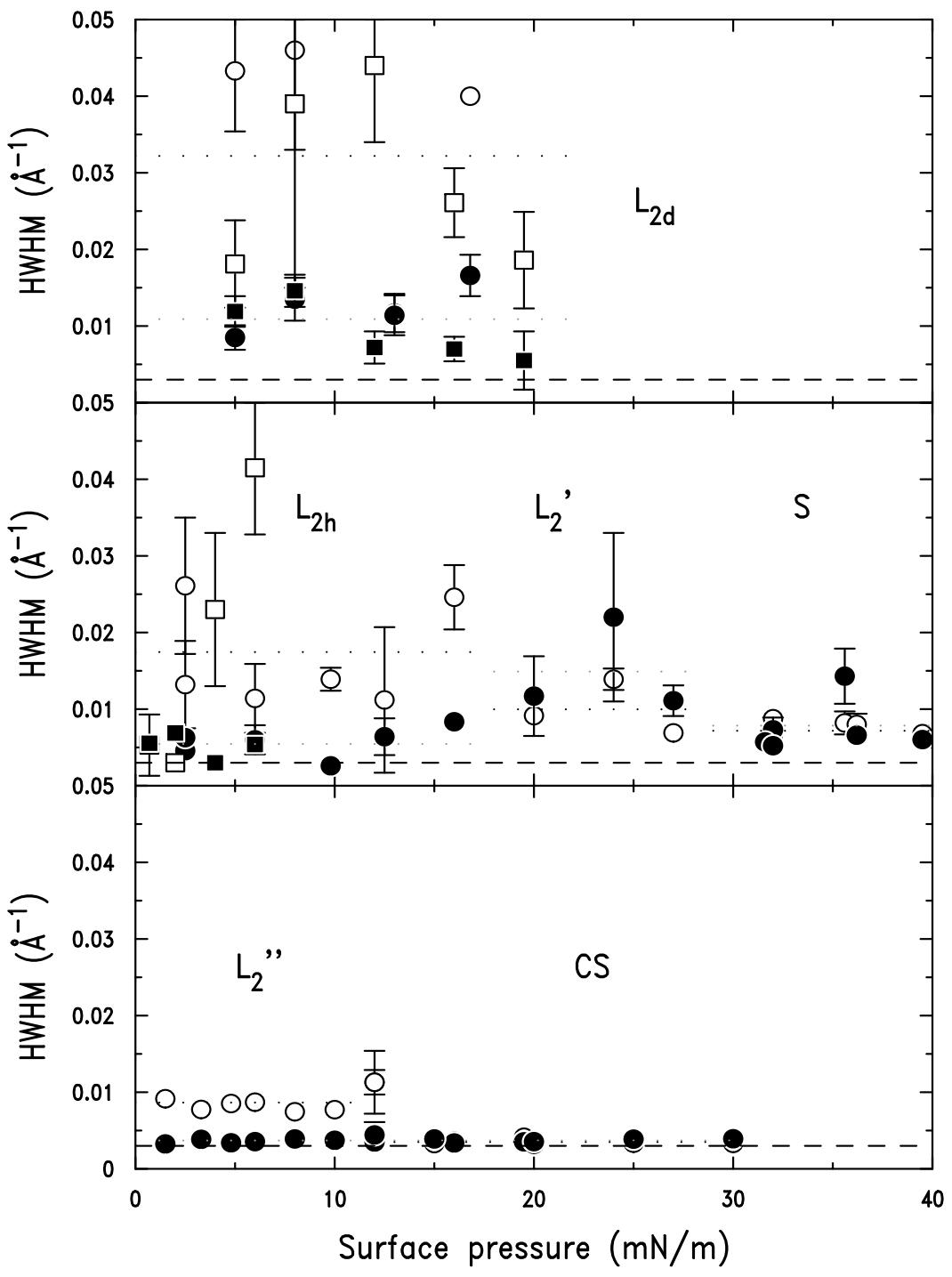
Fig. 7
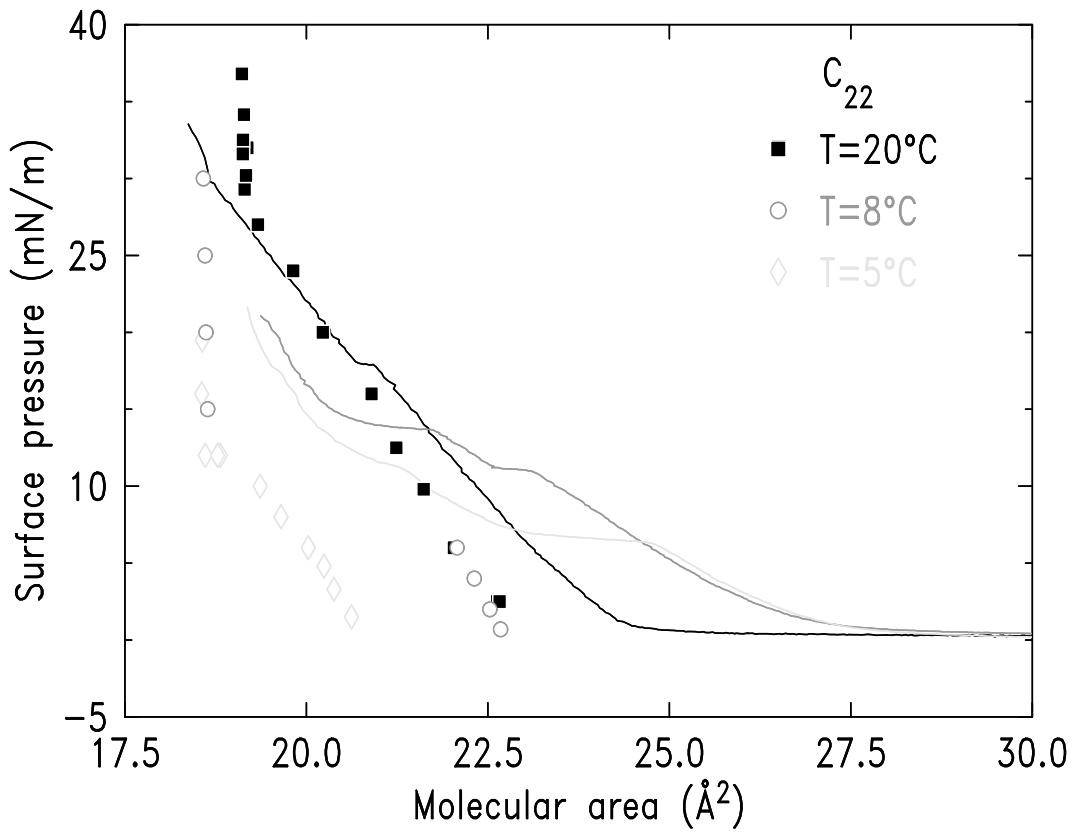
Fig. 8

Fig. 9

Fig. 10

PHB

25 ^{O}

20 ^{O}

HB

33 ^{O}

45 ^{O}
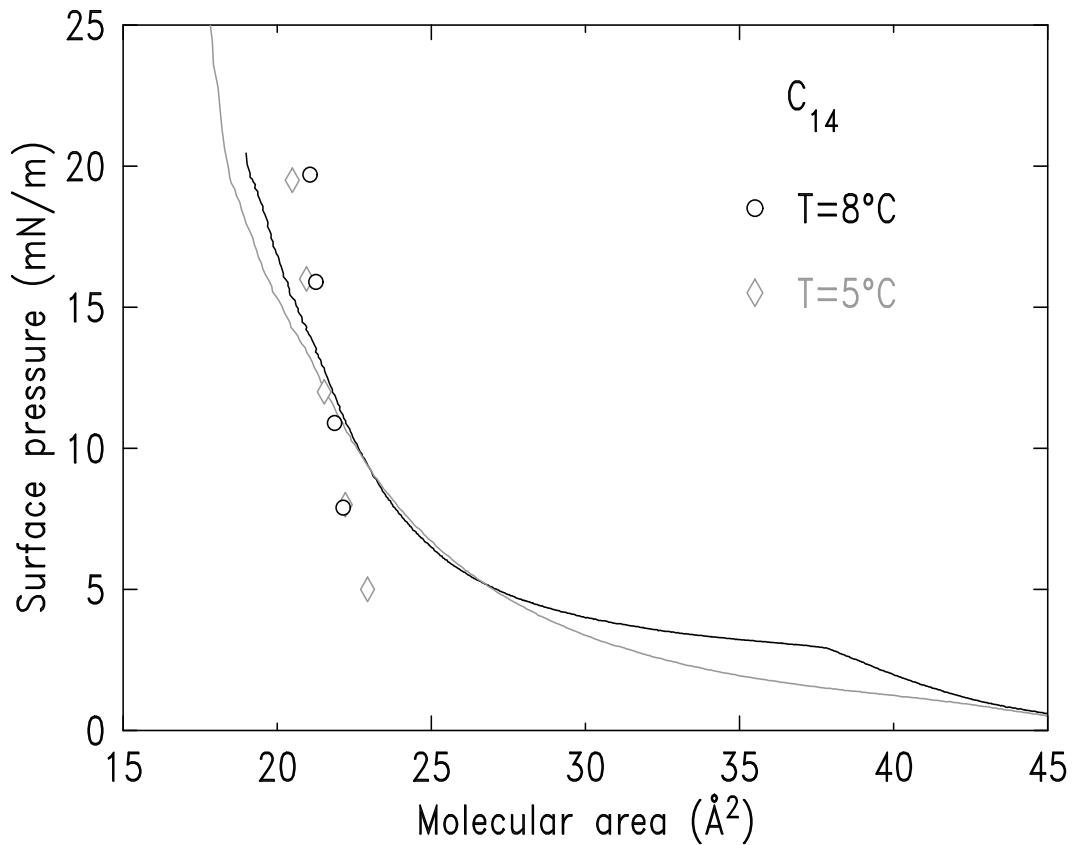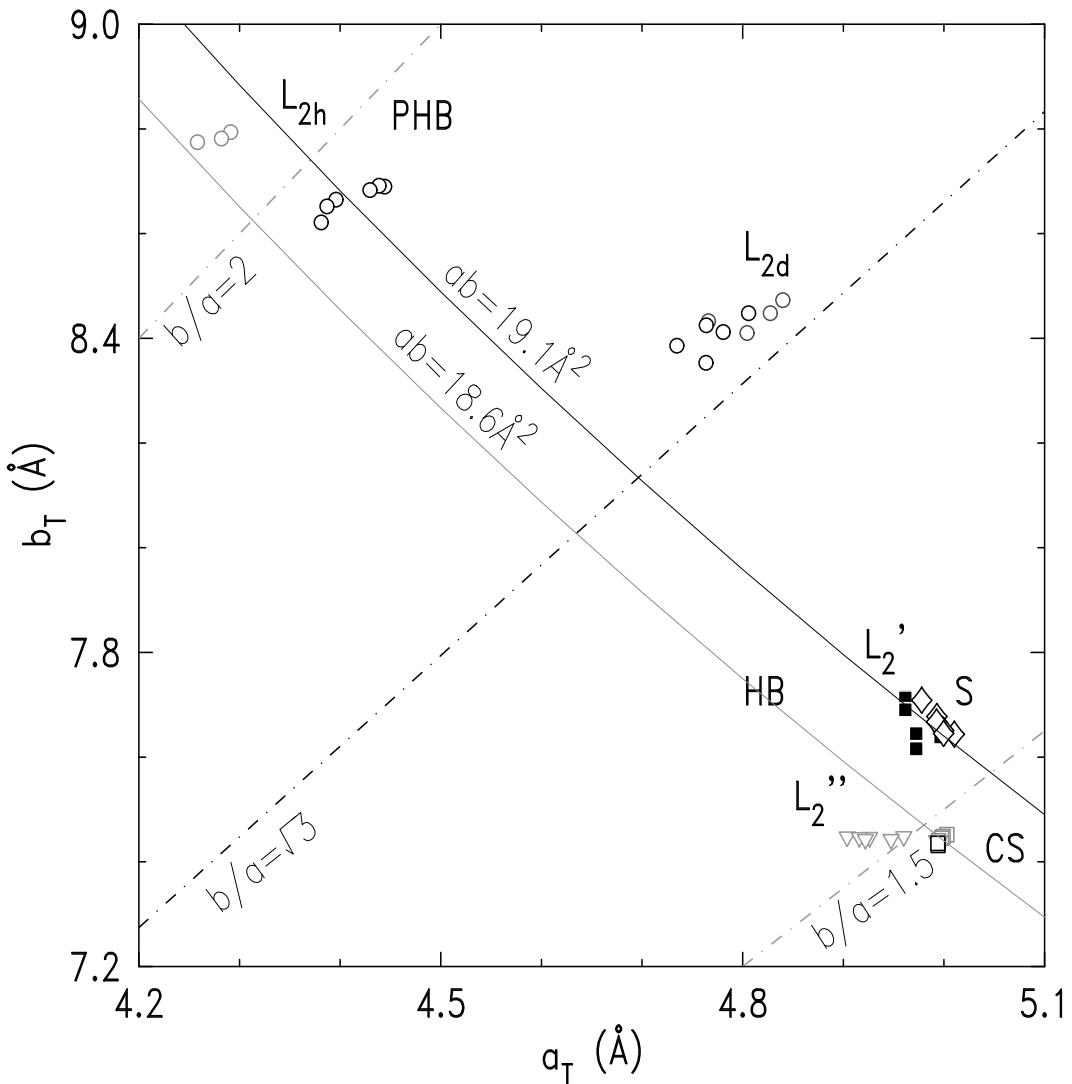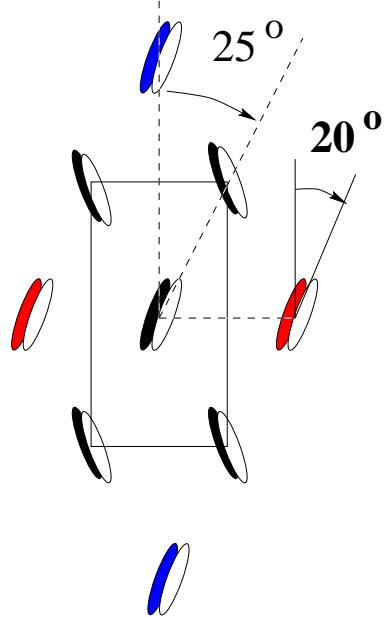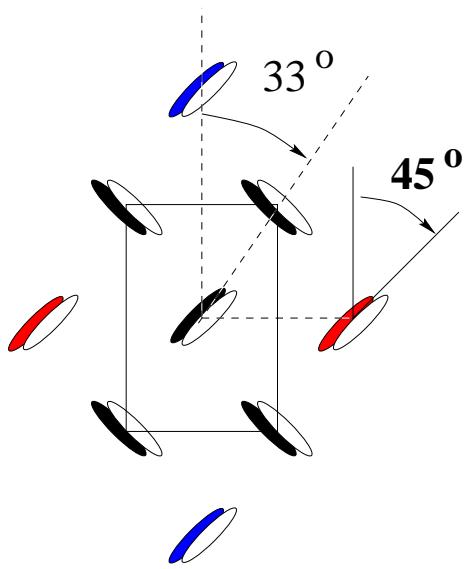
Fig. 11
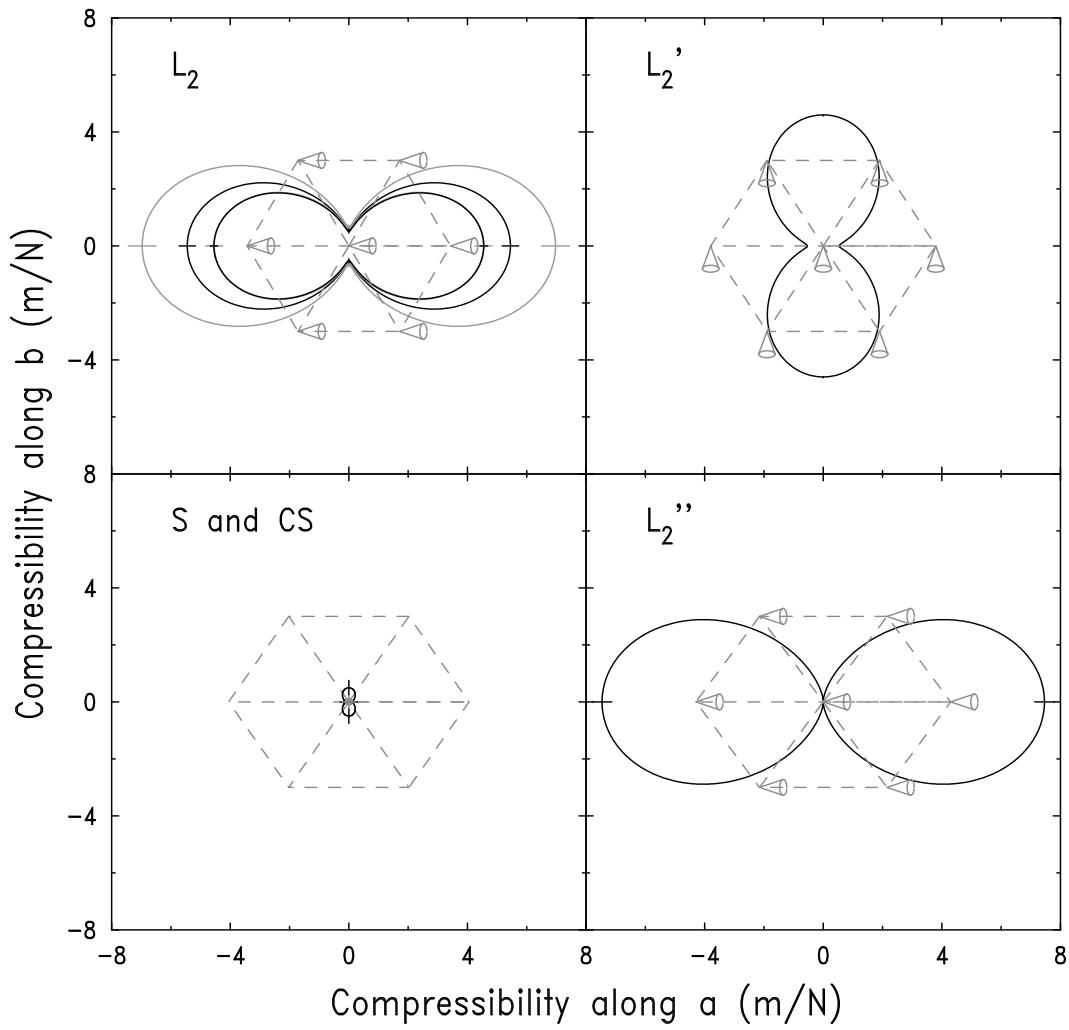
Fig. 12

Fig. 13

Fig. 14

Fig. 15

Fig. 16

(a)

(b)

(c)

Fig. 17